Polyrotaxanes

DOI: 10.1002/anie.201301397

Synthesis of Paclitaxel-Conjugated β-Cyclodextrin Polyrotaxane and Its Antitumor Activity**

Shuling Yu, Yajun Zhang, Xin Wang, Xu Zhen, Zhaoheng Zhang, Wei Wu, and Xiqun Jiang**

Cyclodextrin (CD) polyrotaxanes (PRs), formed generally by threading multiple CD rings onto a polymer chain with bulky end-caps, have many fascinating features by virtue of their unique structures and chemical compositions.[1] Depending on the length of the polymer axle and the number of CD rings threaded, the PRs have tunable molecular size.[1c] The abundant hydroxy groups on the CD moiety make it possible to incorporate various functional molecules, improving the overall properties and extending the applications of the PRs.[2,3] The mobility of CD rings on the polymer axle can effectively enhance the interactions between the receptors on cell surfaces and PR-bound ligands through the spatial adjustability of the PRs to fit external changes.[2,4]

These properties of CD PRs combined with the good biocompatibility and biodegradability of CD molecules enable the PRs to be very promising in drug delivery. Unfortunately, we still know little about their biological effects, especially in vivo behaviors, such as pharmacokinetics, biodistribution, and diffusion in a tumor matrix. In addition, although the accumulation of nanomaterials in tumors can be achieved by the enhanced permeability and retention (EPR) effect,[5] the abnormal architecture and composition of tumors, such as accumulated solid stress, abnormal blood vessel networks, elevated interstitial fluid pressure (IFP), and a dense interstitial structure, make the diffusion of nanomaterials (tens- to 100 nm in diameter) in tumor tissues very limited and consequently hamper the delivery of drugs throughout the tumor tissue in a concentration sufficient to be therapeutic. CD PRs have a size of several nanometers, and thus may offer good penetration in tumors because the penetration of nanomaterials in tumor tissues increases with decreasing material size.[6]

To date, although many types of α-CD PRs with various end-capping groups has been synthesized,[1a,2,7,8] only a few successful cases of β- and γ-CD PR preparations have been reported owing to the difficulty in effective end capping. Harada and co-workers successfully prepared β-CD PRs by a photoinduced Diels–Alder reaction of supramolecular complexes between β-CD and poly(propylene glycol) (PPG) having a triphenylmethyl group at one end and a 2-anthryl group at the other end, after they had tried different bulky stoppers.[9] By using a similar photoreaction, γ-CD PRs were prepared from a supramolecular complex between γ-CD and PPG having 9-anthryl groups at both ends.[10] Li and co-workers prepared β-CD PRs by selectively complexing β-CD with the central PPG block of a pluronic triblock copolymer and then capping the supramolecular complex with two 2,4,6-trinitrobenzene sulfonate molecules at each end.[3]

Herein, we present an effective preparation of β-CD PR by using PPG terminated by alkynyl groups (dialk-PPG, Scheme 1, the number average molecular weight of the PPG segment is ca. 2000) as the axle and mono-(6-azido-6-deoxy)-β-cyclodextrin (β-CD-N_3, Scheme 1) as the end-capping

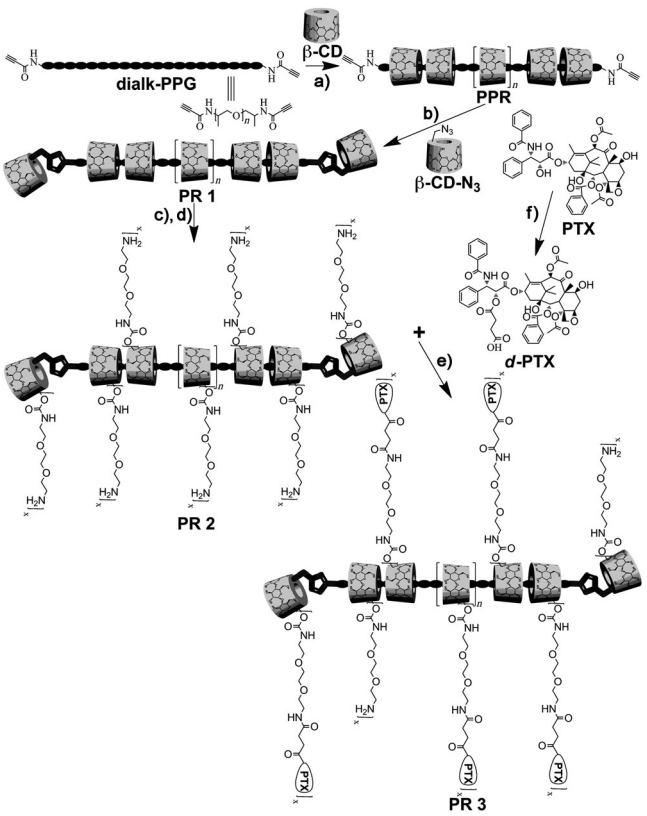

Scheme 1. Synthesis of β-CD PR and its derivatives. a) water, methanol, b) 1,1,4,7,7-pentamethyldiethylenetriamine (PMDETA), $CuSO_4 \cdot 5H_2O$, sodium L-ascorbate, water, c) 1,1′-carbonyldiimidazole (CDI), DMSO, d) diaminotri(ethylene glycol), DMSO, e) *N*-(3-*d*imethylaminopropyl)-*N*′-ethylcarbodiimide hydrochloride (EDC×HCl), *N*-hydroxysuccinimide (NHS), triethylamine, DMSO, f) succinic anhydride, pyridine.

[*] S. L. Yu, Y. J. Zhang, X. Wang, X. Zhen, Z. H. Zhang, Dr. W. Wu, Prof. X. Q. Jiang
Laboratory of Mesoscopic Chemistry and Department of Polymer Science & Engineering, College of Chemistry & Chemical Engineering, Nanjing University
Nanjing, 210093 (P. R. China)
E-mail: wuwei@nju.edu.cn
jiangx@nju.edu.cn

[**] This work was supported by the Natural Science Foundation of China (Nos. 51033002 and 51273090).

Supporting information for this article is available on the WWW under http://dx.doi.org/10.1002/anie.201301397.

reagent. After the complexation of β-CD with dialk-PPG polymer chains, the capping reaction of alkyne–azide 1,3-dipolar cycloaddition was carried out in aqueous medium to cap the polypseudorotaxane (PPR, Scheme 1), affording PR **1** (Scheme 1). Subsequently, the conjugation of paclitaxel (PTX, antitumor agent) and PR **1** was performed through a hydrophilic spacer of diaminotri(ethylene glycol) and a biodegradable ester linkage. The cellular uptake, cytotoxicity, biodistribution, penetration in tumor and antitumor performance of the PR-PTX conjugate (PR **3**) were investigated. Encouragingly, a unique in vivo fate, significant antitumor response, and deep intratumoral penetration of PR-PTX were observed.

PR **1** was structurally characterized by ^{1}H NMR spectroscopy. Figure 1 a shows the spectra of PR **1** and its precursor PPR in [D$_6$]DMSO. Compared to PPR, the proton signals from PR **1** are broad and unresolved, indicating that the supramolecular architecture of PR **1** is stable in DMSO and the rotaxanation decreases remarkably the conformational flexibility of CD and dialk-PPG moieties, causing the broadening of the signals. In contrast, PPR is not stable in DMSO and CDs dethread from the polymer axle to yield a mixture of separated CDs and dialk-PPG, leaving their proton signals narrow. By comparing the integral intensity of the C(1)H signal of β-CD with that of the methyl proton on dialk-PPG, the stoichiometry of PR **1** can be calculated to be about 1:3 (β-CD:propylene glycol unit), meaning that about 11 β-CD molecules are locked on one polymer axle.

Two-dimensional diffusion-ordered NMR spectroscopy (2D DOSY) spectrum of PR **1** was compared with that of PPR. The spectrum of PPR (Figure S1 in Supporting Information) shows two separate peaks corresponding, respectively, to β-CD and PPG along the diffusion axis, and all β-CD proton signals are associated with a diffusion coefficient (D) of about 1.23×10^{-10} m^{2}s^{-1}, while the PPG exhibits a smaller D of about 9.77×10^{-11} m^{2}s^{-1}, suggesting that the PPR has decomposed into its two separate components, β-CD and dialk-PPG by dethreading in DMSO. In contrast, in the 2D DOSY spectrum of PR **1** (Figure 1 b), all the proton signals from β-CD and dialk-PPG are correlated with the same D of about 3.55×10^{-11} m^{2}s^{-1} and a single peak corresponding to the D value can be found along the diffusion axis, revealing that the two components really move as a whole unit and the supramolecular structure of PR **1** is stable in DMSO.

2D rotating-frame Overhauser effect spectroscopy (2D ROESY) of PR **1** confirmed the supramolecular structure (Figure 1 c). A strong cross-peak arising from the non-bonding interaction between the methyl protons (δ = 1.04 ppm) of the dialk-PPG and the C(3)H (δ = 3.65 ppm) and C(5)H (δ = 3.55 ppm) protons of the β-CD units is observed, indicating that the CD rings are really threaded onto the polymer axle and the supramolecular structure is successfully stabilized by the end-capping groups.

The morphological structure of PR **1** was examined by high-resolution transmission electron microscopy (HR-TEM, Figure S2 in Supporting Information), which shows a near-spherical shape with diameter of approximately 2.0 nm for the PR **1**. This observation is consistent with other work which demonstrates that PRs composed of α-CD and PEG behave as random coils in good solvents.[11]

To couple PTX with PR **1**, a succinate-based PTX ester derivative (*d*-PTX, Scheme 1) was synthesized.[12] Thereafter, the *d*-PTX was covalently linked to PR **1** in a three-step reaction, including activation of the hydroxy groups on PR **1** by CDI, introduction of amino groups by using excess diaminotri(ethylene glycol) (affording PR **2**, Scheme 1), and conjugation of PR **2** with *d*-PTX by amidation under the activation with EDC × HCl and NHS (affording PR **3**, see Figure S3 and S4 in Supporting Information for the ^{1}H NMR spectra of PR **2** and **3**). The amounts of free amino groups on PR **2** and **3** were

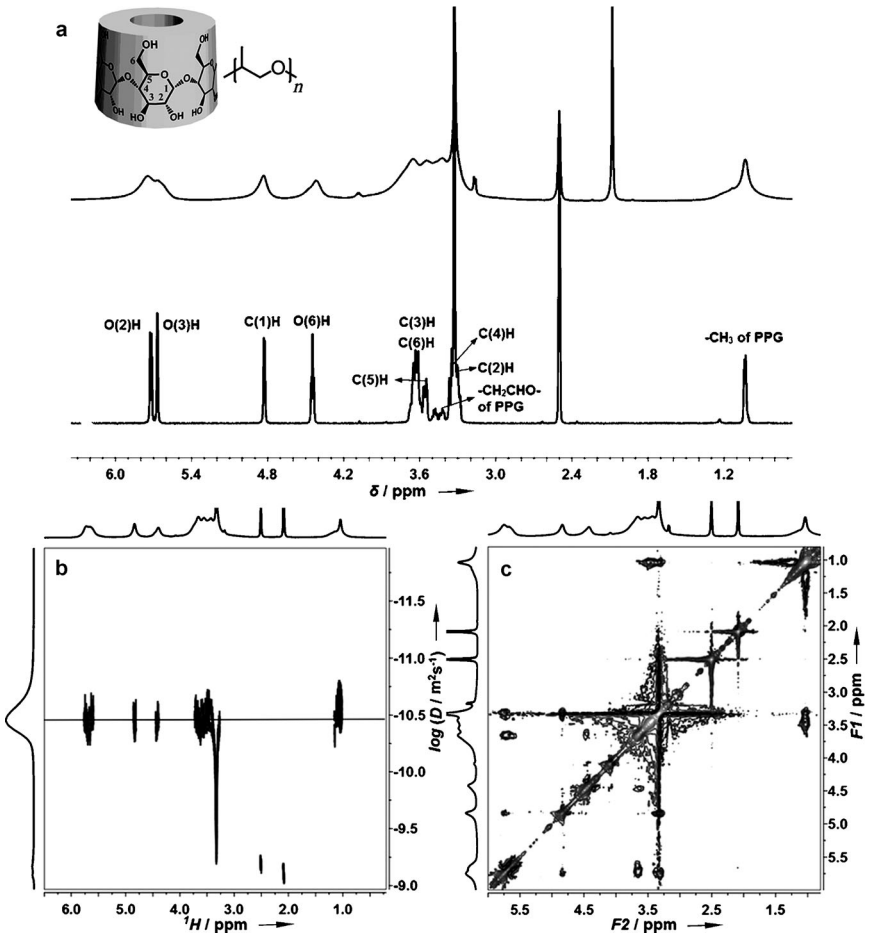

Figure 1. a) ^{1}H NMR spectra of PR **1** (top) and its precursor PPR (bottom); b) 2D DOSY spectrum of PR **1**; c) 2D ROESY spectrum of PR **1** in [D$_6$]DMSO.

determined to be approximately 0.55 and 0.05 mmol g^{-1}, respectively, by ninhydrin assay,[13] indicating that the average number of amino groups per CD in PR **2** and PTX per CD in PR **3** are around 0.80 and 0.73, respectively, and that about 90% of the amine groups in PR **2** are modified by *d*-PTX. Accordingly, the drug-loading content of PR **3** was calculated to be approximately 29% at a weight percent of conjugated PTX to PR **3** (see Supporting Information for the calculation method), which is consistent with the ^{1}H NMR spectrum of PR **3**.

Since there is an ester linkage between the PR and PTX moieties in PR **3** that is hydrolytically unstable, the PTX bound to PR should be released in aqueous medium by the hydrolysis of the ester bonds. The in vitro PTX release profiles of PR **3** in different media at 37 °C show that the PTX release is faster at pH 5.0 than at pH 7.4 in buffer solutions (Figure S5 in Supporting Information). However, over the 72 h monitoring duration, the amount of PTX released does not exceed 11% of the total amount of the loaded drug, suggesting the relatively high stability of the ester bond in the absence of an enzyme. In contrast, a much faster PTX release is found in fetal bovine serum (FBS), which can be attributed to the catalysis by the esterase in the serum.

Confocal laser scanning microscopy (CLSM) was used to trace the cellular uptake of PR **3** after labeling PR **3** with FITC through the reaction of the remnant amino groups on PR **3** with the isothiocyanate group on the dye. Figure S6 shows a typical CLSM image of human neuroblastoma SH-SY5Y cells co-incubated with FITC-labeled PR **3** at 37 °C for 4 h. The labeled PR **3** is easily internalized by SH-SY5Y cells at 37 °C and the cells retain their normal morphology after the incubation. We also investigated the cellular uptake of the FITC-labeled PR **3** by using the same cell line at 4 °C where endocytosis should not occur, and found that PR **3** could not enter the cells, indicating that PR **3** is internalized by the cells by an endocytosis process.

To evaluate the pharmacological activity of PR **3** and the potential toxicity of plain PRs (PR **2**), the in vitro cytotoxicities of PR **3** and **2** against SH-SY5Y cells were determined with a positive control of commercial Taxol (Figure S7 in Supporting Information). As shown in Figure S7a, PR **3** exhibits slightly lower cytotoxicity than Taxol at equal PTX concentrations, which is consistent with the sustained drug-release properties of PR **3**. Furthermore, this examination also demonstrates that PTX is still pharmacologically active after the conjugation and release processes and PR **2** does not exhibit significant cytotoxicity at concentrations up to 500 μg mL^{-1} (Figure S7b). The cellular uptake of FITC-labeled PR **3** and the cytotoxicities of PR **2** and **3** on murine hepatoma H22 cells were also investigated and show similar results to SH-SY5Y cells (Figure S8 and S9 in Supporting Information).

To understand the fate of PR **3** in the living body, a non-invasive real-time near-infrared fluorescence (NIRF) imaging technique was used to study its distribution in tumor-bearing mice after labeling PR **3** with a near-infrared (NIR) dye (NIR-797) through the reaction of the amino groups on PR **3** with the isothiocyanate group on the dye. Figure 2a shows the time-dependent NIRF images of a hepatic H22 tumor-bearing

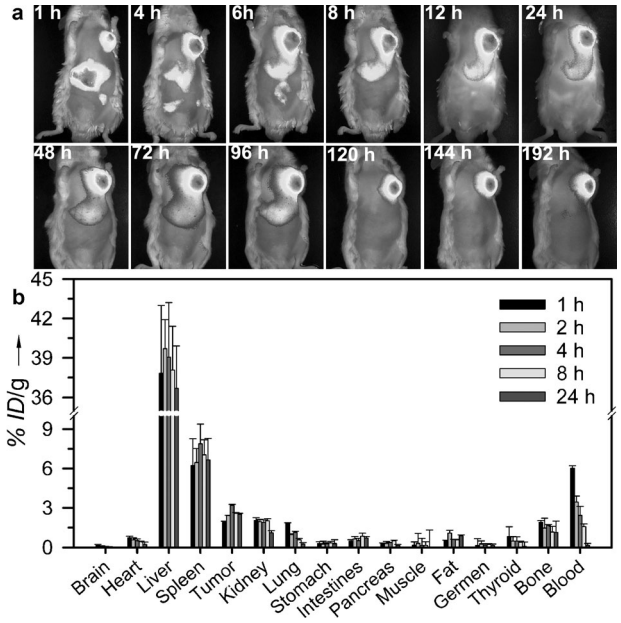

Figure 2. a) In vivo NIRF images of a tumor-bearing mouse at different time points after injecting the NIR-797-labeled PR **3** in the tail vein. b) Biodistribution of ^{99m}Tc-labeled PR **3** in different organs of tumor-bearing mice at different times after tail-vein injection acquired by gamma scintillation counting as the percentage of ID per gram of collected organs and based on five mice per group. This Figure is shown in color as Figure S10 in Supporting Information.

mouse after injecting the labeled PR **3** via the tail vein. From these images, it can be seen that the fluorescence signal is mainly distributed in the regions of liver and tumor within 96 h post injection (p.i.). After 96 h p.i., the fluorescence signal can only be observed in the tumor region, indicating that PR **3** can be eliminated by the hepatobiliary systems and importantly can accumulate in the tumor through the EPR effect. It is notable that there is still a strong fluorescence signal in tumor region at 192 h p.i., suggesting the long retention of the modified PR in the tumor, which is very favorable for the therapeutic action of PR **3**. However, because of the planar image and different depth of the organs, the fluorescence signal in different organs cannot be compared. In view of this, the main organs including heart, liver, spleen, lung, kidney, stomach, brain, intestine, and tumor were excised at the completion of the 192 h in vivo imaging and imaged (Figure S11 in Supporting Information). As expected, the fluorescence signals can be observed in tumor and liver, and the intensity in tumor is much stronger than that in liver.

Although NIRF imaging can be used to monitor the in vivo fate of a NIR probe over a relatively long period, it is difficult to analyze the signals from different organs due to the limited penetration depth of NIR signal. To evaluate the biodistribution of PR **3** more accurately, we labeled PR **3** with radioactive nuclide technetium-99 m (^{99m}Tc) by introducing diethylenetriaminepentaacetic (DTPA) chelator to PR **3** through the reaction of the amino groups on PR **3** with DTPA dianhydride followed by complexing with ^{99m}Tc ($T_{1/2}$ = 6.02 h, E_γ = 141 keV).

The distribution of the ^{99m}Tc-labeled PR **3** in tumor-bearing mice was quantitatively studied by gamma scintillation counting analyses of the dissected organs from hepatic H22 tumor-bearing mice at different times after injecting ^{99m}Tc-labeled PR **3** via tail vein (Figure 2b). As expected, among the collected tissues, the liver shows the highest concentration of ^{99m}Tc-labeled PR **3**, followed by the spleen. This is caused by the osponization-induced reticuloendothelial system (RES) capture. Figure S12 (in Supporting Information) depicts the time-dependent variation of the ^{99m}Tc-labeled PR **3** concentration in blood, tumor, and body of mice based on gamma scintillation counting. The half-life of the labeled PR **3** in blood circulation is calculated to be around 5.8 h (Figure S12a, see Supporting Information for the calculation method), much longer than that reported for Taxol (18.8 ± 1.5 min).[14] The long blood circulation time of the labeled PR **3** should greatly facilitate its accumulation in the tumor. Consistent with the results of NIRF imaging, significant accumulation of the labeled PR **3** in the tumor is also demonstrated by the gamma scintillation counting analyses. The maximum of tumor uptake of all the times tested is approximately 3.2% ID/g at 4 h p.i., and the level slightly decreased to about 2.5% ID/g at 24 h p.i. (Figure S12b). Furthermore, as shown in Figure S12c, the labeled PR **3** is excreted slowly and there is approximately 69% ID remaining in the mouse body at 24 h p.i.

The in vivo antitumor performance of PR **3** was assessed by using subcutaneous hepatic H22 tumor-bearing mice as mode animals and was compared with that of Taxol with a dosage of 10 mg of PTX equivalent (equiv) per kilogram of body weight every four days. PR **2** (containing the same PR concentration as PR **3**) and saline-treated groups were used as controls. After the treatments, the tumor volumes and survival rates of all the test groups were examined. The tumor volume evolution after the treatments with PR **3**, Taxol, PR **2** and saline are shown in Figure 3a. It can be seen that both the PTX formulations (PR **3** and Taxol) exhibit significant antitumor activity. The PR **3**-treated group shows the slowest tumor growth rate among all the test groups. From the 5th day p.i., the relative tumor volumes obtained from the groups treated with PR **3** and Taxol show a statistically significant difference ($P < 0.05$) and on the 15th day p.i., the tumor growth inhibition calculated for the group treated with PR **3** is 78.7%, while for the Taxol-treated group, the value is 30.7% (see Supporting Information for the calculation method), indicating that PR **3** has much better tumor suppression effect than Taxol. There is no statistically significant difference in relative tumor volumes between the groups treated with PR **2** and saline, showing that PR **2** does not have any antitumor activity. The body weights (Figure S13 in Supporting Information) and clinical situations of all the test groups were scrutinized and did not appear to be influenced by the treatments of either the two PTX formulations or PR **2** when compared to the saline-treated group, indicating the well-tolerated dose level of drug and negligible toxicity of PR imposed on the experimental mice.

Animal survival in each test group was recorded and shown in Figure 3b. All the mice treated with saline, PR **2** and Taxol died within 56 days after the treatments, in contrast,

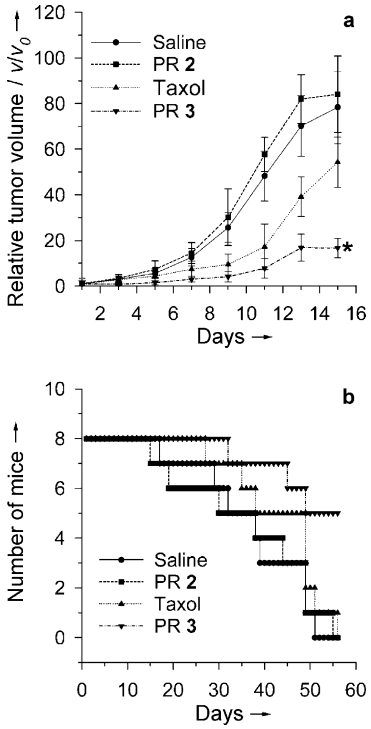

Figure 3. a) In vivo antitumor effect obtained from each treated group, expressed as the average values of the relative tumor volume v/v_0 (where v denotes the tumor volume at test time points and v_0 denotes the corresponding initial tumor volume at the beginning of treatment). $^*P < 0.05$ (versus Taxol-treated group from the 5th day). b) Kaplan–Meier curves showing survival of tumor-bearing mice in various groups.

only 3 of 8 mice died in the PR **3**-treated group within the same period. The median survival times for saline, PR **2** and Taxol-treated groups are 38, 38 and 49 days, respectively, whereas, the median survival time for PR **3**-treated group exceeds 61 days and is much longer than other test groups.

To further gain insight into the antitumor performance of PR **3**, we examined the apoptosis and proliferation levels in the tumors treated by different formulations, including multiple-dose (10 mg kg^{-1} PTX equiv every other day, three times totally) and single-dose (10 mg kg^{-1} PTX) PR **3**, Taxol (10 mg kg^{-1} PTX), PR **2**, and saline, by using TUNEL and PCNA assays respectively (Figure S14 in Supporting Information). On the 7th day post treatments, the mice were sacrificed and the tumors were resected. After a standard staining process, the tumor slices were analyzed by optical microscopy (Figure S14a). It can be seen that the percentage of apoptosis cells determined by TUNEL assay in tumors treated by single-dose PR **3** is significantly higher than that in tumors treated by single-dose Taxol (11.67 ± 1.03% versus 7.86 ± 2.04%, $P < 0.05$, Figure S14b) and repeated administration of PR **3** induces a significant increase in apoptosis level (18.25 ± 3.33%). PR **2**-treatment does not cause significant difference in apoptosis level when compared to saline-treated group. Furthermore, in the case of PCNA assay that determines the proliferation active cells, high proliferation levels are observed in saline and PR **2**-treated groups. Comparing to the Taxol-treated group, the percentage of

PCNA-positive cells significantly decreases in the single-dose PR **3**-treated group and increasing treatment times can further reduce the proliferation level. Based on these immunohistochemical analyses, it is reasonable to conclude that conjugating PTX to PRs can greatly improve its ability to induce apoptosis and inhibit proliferation in tumor.

To evaluate any unwanted side effects of PR **3**, histological analyses of the groups treated with single-dose and multiple-dose PR **3**, Taxol, PR **2** and saline were conducted on the 7th day post treatments. As shown in Figure S15, histological slices of heart, liver, spleen, lung, and kidney show that none of the treatments cause any significant lesion to the tested organs, suggesting the low toxicity of PR **3** even to the high PR **3**-uptake organs (i.e. the liver) at least in the short-term.

The EPR effect allows nanomaterials to preferentially accumulate in tumors. Nevertheless, the abnormal physiological characteristics of tumor tissue, greatly hinder drug transport in tumor tissue and restrict the drug-loaded nanomaterials around blood vessels. In this case, diffusion becomes the primary mode for drug transport throughout the entire tumor. We investigated the penetration of FITC-labeled PR **3** in tumors by using CLSM for tumor slice observation and fluorescence in vivo endomicroscopy (FIVM) for living subject microscopic imaging. Figure 4 shows representative CLSM images of the slices of H22 tumor tissues dissected at 5, 9, and 24 h after tail-vein injection of the labeled PR **3**. The red fluorescence signal arises from Alex-594-conjugated

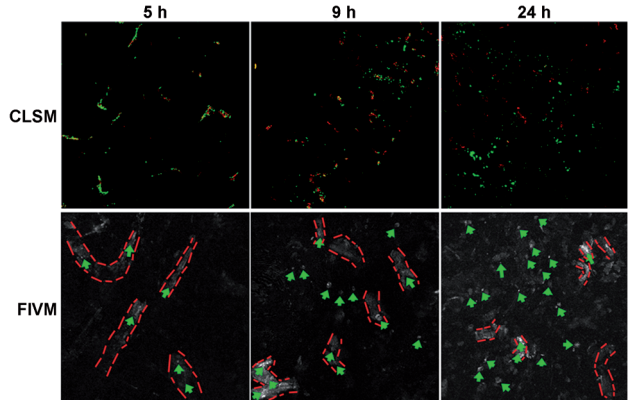

Figure 4. Penetration of FITC-labeled PR **3** in tumor tissues observed by CLSM (red and green signals are from stained blood vessels and FITC-labeled PR **3**, respectively) and FIVM (blood vessels and FITC-labeled PR **3** are indicated by red dashed lines and green arrows, respectively).

secondary antibody complexed with primary rat anti-mouse CD31 antibody, which corresponds to the location of blood vessels. The green fluorescence signal is from the FITC-labeled PR **3**. It can be seen that at 5 h p.i., most of the labeled PR **3** is restricted in or around the tumor blood vessels, and at 9 h p.i., more green signals can be observed outside the blood vessels indicating the extravasation of the labeled PR **3** even if the translocation distances are not large. Further, at 24 h p.i., most of the green signals are observed outside the blood vessels and distributed in a large area in tumor tissue. These results suggest that the labeled PR **3** can leak out of the tumor blood vessels and penetrate relatively deep in the tumor interstitium. The FIVM allows microscopic imaging of tumor tissue in vivo and thus provides a nondestructive and straightforward way to investigate the penetration in tumors (Figure 4). The locations of the labeled PR **3** and tumor vessels are marked in the images. The extravasation and gradual diffusion of the labeled PR **3** in tumor can also be observed, which is well consistent with the results of CLSM imaging. On the basis of our previous penetration studies on polymeric nanoparticles with diameters of 40–54, 90 and 257 nm,[15] the labeled PR **3** has significantly better diffusion properties in tumor tissue than polymeric nanoparticles.

In conclusion, we synthesized β-CD PRs with dialk-PPG as axle and β-CD-N_3 as end-capping group, in which about 11 β-CD molecules are locked on one axle. Through the hydroxy groups on the PR and a hydrophilic spacer, a succinate-based PTX ester derivative was attached to the PR covalently. The PR-PTX conjugate (PR **3**) has a desirable drug loading content of about 29% and the PTX release can be accelerated by esterase catalysis. The in vitro experiments demonstrate that the PR **3** can be internalized readily by tumor cells and retain the pharmacological activity of PTX. The biodistribution, antitumor performance, and penetration in tumors of the PR-PTX conjugate demonstrate that it has significantly superior efficacy in impeding tumor growth and prolonging the lifetime of tumor-bearing mice relative to Taxol.

Received: February 17, 2013
Revised: April 14, 2013
Published online: June 5, 2013

Keywords: antitumor agents · β-cyclodextrin · biodistribution · paclitaxel · polyrotaxanes

[1] a) J. Araki, K. Ito, *Soft Matter* **2007**, *3*, 1456–1473; b) G. Wenz, B. Keller, *Angew. Chem.* **1992**, *104*, 201–204; *Angew. Chem. Int. Ed. Engl.* **1992**, *31*, 197–199; c) A. Harada, A. Hashidzume, H. Yamaguchi, Y. Takashima, *Chem. Rev.* **2009**, *109*, 5974–6023.
[2] T. Ooya, M. Eguchi, N. Yui, *J. Am. Chem. Soc.* **2003**, *125*, 13016–13017.
[3] J. Li, C. Yang, H. Z. Li, X. Wang, S. H. Goh, J. L. Ding, D. Y. Wang, K. W. Leong, *Adv. Mater.* **2006**, *18*, 2969–2974.
[4] N. Yui, *Macromol. Symp.* **2009**, *279*, 158–162.
[5] S. Taurina, H. Nehoffa, K. Greish, *J. Controlled Release* **2012**, *164*, 265–275.
[6] a) H. Cabral, Y. Matsumoto, K. Mizuno, Q. Chen, M. Murakami, M. Kimura, Y. Terada, M. R. Kano, K. Miyazono, M. Uesaka, N. Nishiyama, K. Kataoka, *Nat. Nanotechnol.* **2011**, *6*, 815–823; b) S. D. Perrault, C. Walkey, T. Jennings, H. C. Fischer, W. C. W. Chan, *Nano Lett.* **2009**, *9*, 1909–1915; c) L. Tang, T. M. Fan, L. B. Borst, J. J. Cheng, *ACS Nano* **2012**, *6*, 3954–3966.
[7] A. Harada, J. Li, M. Kamach, *Nature* **1992**, *356*, 325–327.
[8] J. Y. Wu, H. K. He, C. Gao, *Macromolecules* **2010**, *43*, 2252–2260.
[9] M. Okada, A. Harada, *Org. Lett.* **2004**, *6*, 361–364.
[10] M. Okada, Y. Takashima, A. Harada, *Macromolecules* **2004**, *37*, 7075–7077.
[11] T. J. Zhao, H. W. Beckham, *Macromolecules* **2003**, *36*, 9859–9865.

[12] H. M. Deutsch, J. A. Glinski, M. Hernandez, R. D. Haugwitqt, V. L. Narayanan, F. M. Suffness, L. H. Zalkow, *J. Med. Chem.* **1989**, *32*, 788 – 792.
[13] K. N. Pearce, D. Karahalios, M. Friedman, *J. Food Sci.* **1988**, *53*, 432 – 436.
[14] Z. Liu, K. Chen, C. Davis, S. Sherlock, Q. Z. Cao, X. Y. Chen, H. J. Dai, *Cancer Res.* **2008**, *68*, 6652 – 6660.
[15] a) D. Ding, J. Wang, Z. S. Zhu, R. T. Li, W. Wu, B. R. Liu, X. Q. Jiang, *ACS Appl. Mater. Interfaces* **2012**, *4*, 1838 – 1846; b) Z. S. Zhu, C. Xie, Q. Liu, X. Zhen, X. C. Zheng, W. Wu, R. T. Li, Y. Ding, X. Q. Jiang, B. R. Liu, *Biomaterials* **2011**, *32*, 9525 – 9535; c) X. Zhen, X. Wang, C. Xie, W. Wu, X. Q. Jiang, *Biomaterials* **2013**, *34*, 1372 – 1382.

